Supporting Information

Cross-α/β Polymorphism of PSMα3 Fibrils

Olivia M. Cracchiolo[a],[+], Dean N. Edun[a],[+], Vincent M. Betti[b], Jacob M. Goldberg[b], and Arnaldo L. Serrano*[a]

[a] Department of Chemistry and Biochemistry, University of Notre Dame
251 Nieuwland Science Hall, Notre Dame, IN 46556
E-mail: arnaldo.serrano@nd.edu

[b] Department of Chemistry, Colgate University
13 Oak Drive, Hamilton, NY 13346

[+] These authors contributed equally to this work

[*] Corresponding Author

Table of Contents

Experimental Methods

Narrow-Band Pump Generation

To perform the Narrow Band (NB) Pump experiments, we use the capabilities of our AOM to mask all frequencies of the pump beam, leaving only a 3 cm^{-1} Gaussian window centered at a chosen pump frequency. This window is scanned with 2.7 cm^{-1} steps in the frequency range from 1600 to 1700 cm^{-1} to produce the pump axis. The window size and scanning steps were chosen to match the pump resolution of the Broad-Band experiments. Spectra were obtained by scanning line by line along the pump axis, in a manner similar to transient pump-probe collection. We used a [1, off, -1, off] phase cycling scheme to isolate the 2D signal from scattered light. Similar phase combinations of phase cycling have been used for other 2DIR applications.[1] After fully assembling the 2D spectrum, it was smoothed along the pump axis using a 4 cm^{-1} Gaussian smoothing window.

Phase Cycling Schemes

We used phase cycling to measure the relative amplitude of pump-light scattered by the sample region being studied, as fibers are strong light scatterers.[2] In practice, our measured data are proportional to the absolute value squared of the sum of all complex valued electric field contributions as shown in equation 1, where E_1 and E_2 are the pump fields, s is a scattering amplitude, E_{LO} is the local oscillator field (which is also the probe in our experiment),[3] and E_{sig} is the emitted 2DIR signal field.

$$\begin{gathered} I \propto \left|sE_1 + sE_2 + E_{LO} + E_{sig}\right|^2 = \\ (|E|^2 \text{ terms}) + |s|^2 E_1^* E_2 + s^* E_1^* E_{LO} + s^* E_1^* E_{sig} \\ + s^* E_2^* E_{LO} + s^* E_2^* E_{sig} + E_{LO}^* E_{sig} + c.c. \end{gathered} \tag{1}$$

Equation 1 focuses on the cross terms, which are what primarily contribute to or contaminate the 2D spectrum. The heterodyned 2DIR signal, $E_{LO}^* E_{sig}$, is processed to produce 2D spectra, while $\left(s^* E_1^* E_{sig} + s^* E_2^* E_{sig}\right)$ are the smallest terms and can be neglected. The remaining terms require phase cycling to remove.[4–6] Using a pulse shaper-based spectrometer permits shot-to-shot control of the phases of the two pump pulses. By carefully selecting phases and combining measurements, particular signals can be cancelled, which is highly effective at removing these scattered light signals. A typical 4-frame phase cycling scheme is presented in equation 2, where $I_{[\phi_1,\phi_2]}$ represents data where the phases for the first and second pump pulses are set to ϕ_1 and ϕ_2, respectively.

$$S_{2D} \propto \left(I_{[0,0]} + I_{[\pi,\pi]}\right) - \left(I_{[0,\pi]} + I_{[\pi,0]}\right) \tag{2}$$

By combining the phase cycled measurements in this manner, the terms in equation 1 linear in s cancel out entirely. Normally, scattered light is a nuisance to obtaining clean spectra. However, in order to isolate the signal from fibrils, areas with intense light scattering were chosen. To do this, we used the scattered light contamination described above to our advantage by combining the phase cycled measurements according to equation 3. This scheme cancels the 2DIR signal while enhancing $s^* E_1^* E_{LO}$.

$$S_{scat} \propto \left(I_{[0,0]} + I_{[0,\pi]}\right) - \left(I_{[\pi,0]} + I_{[\pi,\pi]}\right) \tag{3}$$

Using S_{scat} we were able to identify sample regions with both large 2DIR signal and large scattering amplitudes (see Figure S3), which we assign to fibrillar samples and from which data in Figures 3 and 4 were collected. Within the conventional 4-frame phase cycling scheme in equation 2, the pump-pump cross term will survive, which, though often neglected due to its $|s|^2$ scaling, is problematic for measuring 2DIR of particularly strong scatterers such as solids. To measure signals associated with fibrils and remove this source of scattering, we employed an 8-frame phase cycling scheme that eliminates this term.[1,7] In the 8-

frame scheme, we used an optical chopper to chop the probe pulse every second laser shot. The 8 frames are combined according to equation 4, where ON and OFF refer to the probe beam. This 8-frame scheme is employed in all 2DIR spectra following the initiation of aggregation (Figure 2a).

$$S_{2D} \propto \{(I_{[0,0,on]} + I_{[\pi,\pi,on]}) - (I_{[0,\pi,on]} + I_{[\pi,0,on]})\} \\ -\{(I_{[0,0,off]} + I_{[\pi,\pi,off]}) - (I_{[0,\pi,off]} + I_{[\pi,0,off]})\} \quad (4)$$

Simulation Methods

Exciton Scattering Matrix Simulations

We used the Nonlinear Exciton Scattering Matrix method developed by Mukamel,[8–10] which avoids the need to diagonalize t2-quantum Hamiltonians. Instead, each vibrational mode is treated as a two-state system where the second excited state manifold is accessed through the mixing between excitons calculated through a scattering matrix. The response is then calculated by summing all combinations of four interactions with light. In principle this results in summing up N^4 interactions, but the complexity can be greatly reduced by pre-determining all interaction strengths between two excitons and only including scatterings where the interaction strength is greater than a defined threshold. Following Mukamel's implementation[11] the exciton overlap factor is defined in equation (5.

$$\eta_{e,e'} = \sum_m |\psi_{e,m}||\psi_{e',m}| \quad (5)$$

We then reject all pairs of interactions where this overlap factor is below 0.55. This number is chosen as it is close to the 0.5 value Mukamel used in demonstrating the effectiveness of the technique while significantly reducing computation time. (For reference, reducing the threshold to 0.5 would effectively double the computation time).

To implement the simulation, first the coordinates for all backbone amide groups in a fibril structure is obtained using coordinates from the crystal structure determined by Landau et al.[12] Then the one-quantum Hamiltonian is built using the Transition Dipole Coupling model.[13] We then diagonalize the one-quantum Hamiltonian to obtain the eigen energies and eigenmodes. Pairs of eigenmodes whose exciton overlap are larger than the chosen threshold are retained. The response functions are calculated in the frequency domain using Green's functions. The response for rephasing, $\mathbb{S}^{k_I}_{\nu_4,\nu_3,\nu_2,\nu_1}(\Omega_3, t_2, \Omega_1)$, and non-rephasing, $\mathbb{S}^{k_{II}}_{\nu_4,\nu_3,\nu_2,\nu_1}(\Omega_3, t_2, \Omega_1)$ pathways are detailed in the following equations where $\Omega_{1,3}$ and t_2 are the corresponding frequency and time grid points over which the spectrum is calculated. The frequency of each exciton i is ϵ_{e_i} while γ_{e_i} is a phenomenological dephasing rate set to 5cm^{-1}. The $\langle \mu^{\nu_4}_{e_4} \mu^{\nu_3}_{e_3} \mu^{\nu_2}_{e_2} \mu^{\nu_1}_{e_1} \rangle$ term is defined in equation (8) where μ_{e_i} is the transition dipole moment of exciton i and $\hat{E}_{\nu_i}$ is a unit vector along the direction of the i^{th} electric field.

$$\mathbb{S}^{k_I}_{\nu_4,\nu_3,\nu_2,\nu_1}(\Omega_3, t_2, \Omega_1) = \\ 2i \sum_{e_4 \ldots e_1} \langle \mu^{\nu_4}_{e_4} \mu^{\nu_3}_{e_3} \mu^{\nu_2}_{e_2} \mu^{\nu_1}_{e_1} \rangle \times I^*_{e_1}(t_2) I_{e_2}(t_2) \mathfrak{T}^*_{e_1}(-\Omega_1) \mathfrak{T}_{e_4}(\Omega_3) \times \Gamma^{ex}_{e_4 e_1, e_3 e_2}(\Omega_3 + \epsilon_{e_1} + i\gamma_{e_1}) \mathcal{J}_{e_3 e_2}(\Omega_3 + \epsilon_{e_1} + i\gamma_{e_1}) \quad (6)$$

$$\mathbb{S}^{k_{II}}_{\nu_4,\nu_3,\nu_2,\nu_1}(\Omega_3,t_2,\Omega_1) =$$

$$2i\sum_{e_4\ldots e_1}\langle\mu^{\nu_4}_{e_4}\mu^{\nu_3}_{e_3}\mu^{\nu_2}_{e_2}\mu^{\nu_1}_{e_1}\rangle\times\ I_{e_1}(t_2)I^{*}_{e_2}(t_2)\mathfrak{T}_{e_1}(\Omega_1)\mathfrak{T}_{e_4}(\Omega_3)\ \times\Gamma^{ex}_{e_4e_2,e_3e_1}(\Omega_3+\epsilon_{e_2}+i\gamma_{e_2})\mathcal{J}_{e_3e_1}(\Omega_3+\epsilon_{e_2}+i\gamma_{e_2}) \tag{7}$$

$$M^{\nu_4\nu_3\nu_2\nu_1}_{e_4e_3e_2e_1}\equiv\langle(\mu_{e_4}\cdot\hat{E}_{\nu_4})(\mu_{e_3}\cdot\hat{E}_{\nu_3})(\mu_{e_2}\cdot\hat{E}_{\nu_2})(\mu_{e_1}\cdot\hat{E}_{\nu_1})\rangle \tag{8}$$

Where $I_{e'}$, $\mathfrak{T}_{e'}$, and $\mathcal{J}_{e'e''}$ are defined as:

$$I_{e'}(t) = \theta(t)\exp(-i\epsilon_{e'}t-\gamma_{e'}t) \tag{9}$$

Where $\theta(t)$ is the Heaviside function.

$$\mathfrak{T}_{e'}(\omega) = \frac{i}{\omega-\epsilon_{e'}+i\gamma_{e'}} \tag{10}$$

$$\mathcal{J}_{e'e''}(\omega) = \frac{i}{\omega-\epsilon_{e'}-\epsilon_{e''}+i(\gamma_{e'}+\gamma_{e''})} \tag{11}$$

The gamma terms are defined below.

$$\Gamma^{ex}_{e_4e_1,e_3e_2}(\omega) = \sum_{m,n}\psi^{*}_{e_4m}\psi^{*}_{e_1m}\Gamma^{site}_{m,n}\psi_{e_3n}\psi_{e_2n} \tag{12}$$

$$\Gamma^{site}_{m,n}(\omega) = -i\bar{\Delta}_m(\overline{D}^{-1})_{m,n} \tag{13}$$

Where $\bar{D}_{m,n}$ is

$$\bar{D}_{m,n} = \delta_{mn} + i\mathcal{G}_{m,n}\,\bar{\Delta}_n \tag{14}$$

Finally, the Green function, $\mathcal{G}_{m,n}(\omega)$ is as follows.

$$\mathcal{G}_{m,n}(\omega) = \sum_{e',e''} \psi_{e'm}\psi_{e''m}\mathcal{J}_{e'e''}(\omega)\psi^*_{e'n}\psi^*_{e''n} \tag{15}$$

Structural Comparison of α-sheets and cross-α fibrils

PSMs have also been associated with the α-sheet structure[14]. α-sheets are defined by the alignment of all nitrogens and carbonyl groups in the same direction along the backbone as opposed to alternating orientations as seen in β-sheets. Figure S1a shows the select residues of cytosolic phosphatase A2 (PDB ID:1rwl)[15] that adopt the α-sheet conformation[16], while S1b shows the cross-α fibrils of PSMα3 (PDB ID:5i55)[17] observed by Landau et. al[18] Both were obtained via PDB structures.

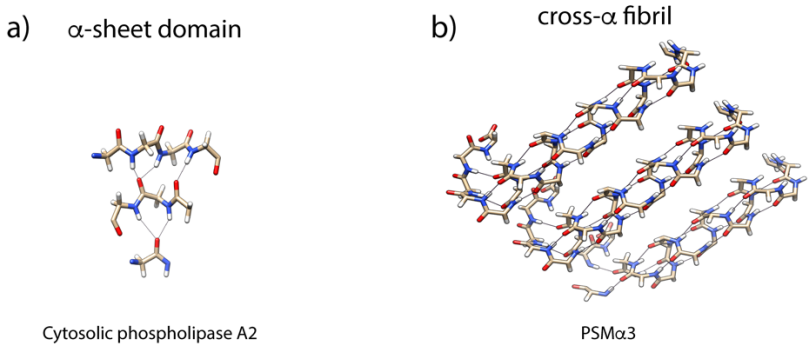

Figure S1. Secondary structures of a) select residues in cytosolic phospholipase A2 that exhibit the α-sheet domain and b) PSMα3 cross-a fibril structure both obtained from crystal structure data.

Transmission Electron Microscopy (TEM)

After incubation the sample was centrifuged at 14,800 rpm for 20 minutes. The supernatant was decanted off and the pellet was resuspended in a 10-fold dilution following the protocol from Landau et al.[17,18] 5 mL of sample was then adhered to a 400-mesh copper TEM grid with Formvar/Carbon support films (Ted Pella, distributed by Getter Group Bio Med, Petah-Tikva, Israel) that had been glow discharged and stained with 2% uranyl acetate. The sample was imaged at 20 keV with 100 nm resolution.

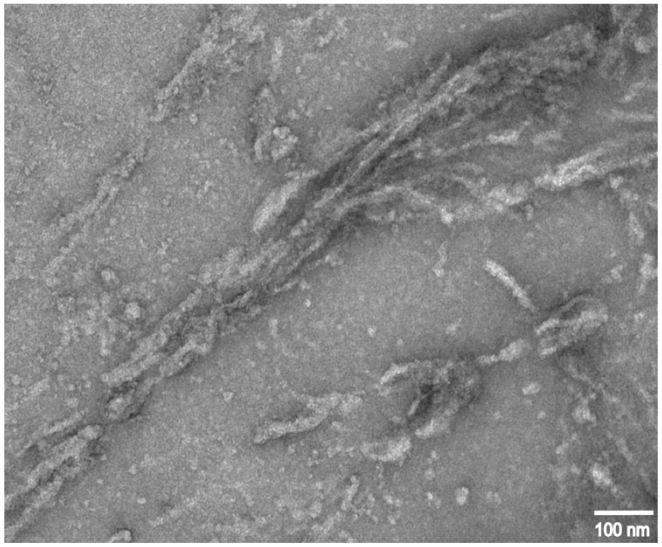

Figure S2. Transmission electron microscopy image of PSMα3 fibrils formed after room temperature incubation. Scale bar indicates 100 nm.

Scattered Light Analysis

To ensure the spectra obtained correspond to fibrils in the sample, a scattering analysis was performed using the time domain data. An alternative phase cycling scheme (given in equation 3 of the main text) was used to maximize scattered light interference signals, which are used as an in-situ measure of the presence of aggregates. The sample in Figure S3a corresponds to the monomeric solution and therefore the scattered light is negligible, while the samples in Figures S3b and c contain fibers, resulting in intense scattered light.

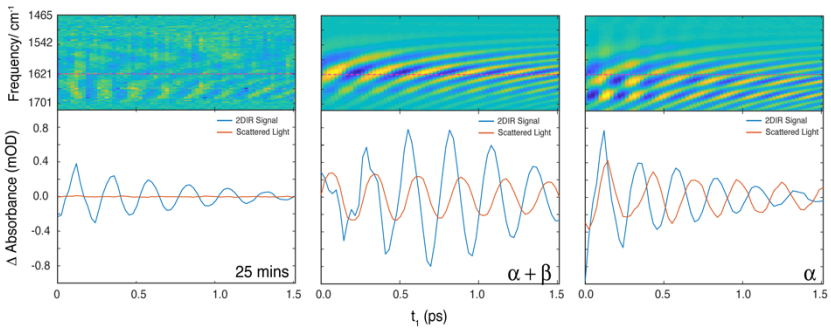

Figure S3. 2DIR signal compared to scattered light. The time domain data for scattered light is depicted in the top panels. The bottom plots show the 2DIR signal (blue) and scattered light (orange) along the horizontal slices (pink dashed line) taken at 1621 cm^{-1} of a) PSMα3 solution after 25 mins, b) the α+β fibrils and c) the isolated cross-α fibril.

Monomer Spectra

Broad Band Pump 2DIR

The BB experiments were performed with 0.5 mM PSMα3 to capture the spectra of the monomer.

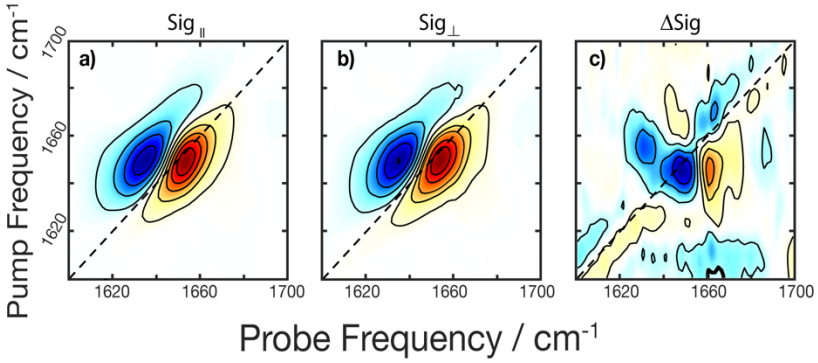

Figure S4. BB 2DIR spectrum of 0.5 mM PSMα3 in D_2O taken with a) parallel b) and perpendicular polarizations using broad band pump. The difference spectrum is shown in c).

References

(1) Baiz, C. R.; Schach, D.; Tokmakoff, A. Ultrafast 2D IR Microscopy. *Optics Express* **2014**, *22* (15), 18724. https://doi.org/10.1364/oe.22.018724.

(2) Hall, D.; Zhao, R.; Dehlsen, I.; Bloomfield, N.; Williams, S. R.; Arisaka, F.; Goto, Y.; Carver, J. A. Protein Aggregate Turbidity: Simulation of Turbidity Profiles for Mixed-Aggregation Reactions. *Analytical Biochemistry* **2016**, *498*, 78–94. https://doi.org/10.1016/j.ab.2015.11.021.

(3) Cracchiolo, O. M.; Geremia, D. K.; Corcelli, S. A.; Serrano, A. L. Hydrogen Bond Exchange and Ca2+Binding of Aqueous N-Methylacetamide Revealed by 2DIR Spectroscopy. *Journal of Physical Chemistry B* **2020**, *124* (32), 6947–6954. https://doi.org/10.1021/acs.jpcb.0c02444.

(4) Shim, S. H.; Strasfeld, D. B.; Ling, Y. L.; Zanni, M. T. Automated 2D IR Spectroscopy Using a Mid-IR Pulse Shaper and Application of This Technology to the Human Islet Amyloid Polypeptide. *Proceedings of the National Academy of Sciences of the United States of America* **2007**, *104* (36), 14197–14202. https://doi.org/10.1073/pnas.0700804104.

(5) Middleton, C. T.; Woys, A. M.; Mukherjee, S. S.; Zanni, M. T. Residue-Specific Structural Kinetics of Proteins Through the Union of Isotope Labeling, Mid-IR Pulse Shaping, and Coherent 2D IR Spectroscopy. *Methods* **2010**, *52* (1), 12–22. https://doi.org/10.1016/j.ymeth.2010.05.002.

(6) Ghosh, A.; Serrano, A. L.; Oudenhoven, T. A.; Ostrander, J. S.; Eklund, E. C.; Blair, A. F.; Zanni, M. T. Experimental Implementations of 2D IR Spectroscopy through a Horizontal Pulse Shaper Design and a Focal Plane Array Detector. *Optics Letters* **2016**, *41* (3), 524. https://doi.org/10.1364/ol.41.000524.

(7) Nishida, J.; Tamimi, A.; Fei, H.; Pullen, S.; Ott, S.; Cohen, S. M.; Fayer, M. D. Structural Dynamics inside a Functionalized Metal-Organic Framework Probed by Ultrafast 2D IR Spectroscopy. *Proceedings of the National Academy of Sciences of the United States of America* **2014**, *111* (52), 18442–18447. https://doi.org/10.1073/pnas.1422194112.

(8) Mukamel, S. *Principles of Nonlinear Optical Spectroscopy*; Lapp, M., Nishizawa, J.-I., Snavely, B. B., Stark, H., Tam, A. C., Wilson, T., Eds.; Oxford University Press: New York, New York, 1998; Vol. 168. https://doi.org/10.3367/ufnr.0168.199805j.0591.

(9) Abramavicius, D.; Palmieri, B.; Voronine, D. V.; Šanda, F.; Mukamel, S. Coherent Multidimensional Optical Spectroscopy of Excitons in Molecular Aggregates; Quasiparticle versus Supermolecule Perspectives. *Chemical Reviews* **2009**, *109* (6), 2350–2408. https://doi.org/10.1021/cr800268n.

(10) Zhuang, W.; Abramavicius, D.; Hayashi, T.; Mukamel, S. Simulation Protocols for Coherent Femtosecond Vibrational Spectra of Peptides. *Journal of Physical Chemistry B* **2006**, *110* (7), 3362–3374. https://doi.org/10.1021/jp055813u.

(11) Zhang, W. M.; Meier, T.; Chemyak, V.; Mukamel, S. Exciton-Migration and Three-Pulse Femtosecond Optical Spectroscopies of Photosynthetic Antenna Complexes. *Journal of Chemical Physics* **1998**, *108* (18), 7763–7774. https://doi.org/10.1063/1.476212.

(12) Salinas, N.; Colletier, J. P.; Moshe, A.; Landau, M. Extreme Amyloid Polymorphism in Staphylococcus Aureus Virulent PSMα Peptides. *Nature Communications* **2018**, *9* (1), 3512. https://doi.org/10.1038/s41467-018-05490-0.

(13) Torii, H.; Tasumi, M. Model Calculations on the Amide-I Infrared Bands of Globular Proteins. *The Journal of Chemical Physics* **1992**, *96* (5), 3379–3387. https://doi.org/10.1063/1.461939.

(14) Bleem, A.; Francisco, R.; Bryers, J. D.; Daggett, V. Designed α-Sheet Peptides Suppress Amyloid Formation in Staphylococcus Aureus Biofilms. *npj Biofilms and Microbiomes* **2017**, *3* (1). https://doi.org/10.1038/s41522-017-0025-2.

(15) Perisic, O.; Fong, S.; Lynch, D. E.; Bycroft, M.; Williams, R. L. Crystal Structure of a Calcium-Phospholipid Binding Domain from Cytosolic Phospholipase A2. *Journal of Biological Chemistry* **1998**, *273* (3), 1596–1604. https://doi.org/10.1074/jbc.273.3.1596.

(16) Armen, R. S.; Alonso, D. O. V.; Daggett, V. Anatomy of an Amyloidogenic Intermediate. *Structure* **2004**, *12* (10), 1847–1863. https://doi.org/10.1016/j.str.2004.08.005.

(17) Tayeb-Fligelman, E.; Tabachnikov, O.; Moshe, A.; Goldshmidt-Tran, O.; Sawaya, M. R.; Coquelle, N.; Colletier, J.-P.; Landau, M. The Cytotoxic Staphylococcus Aureus PSMα3 Reveals a Cross-α Amyloid-like Fibril. *Science* **2017**, *355* (6327), 831–833. https://doi.org/10.1126/science.aaf4901.

(18) Tayeb-Fligelman, E.; Salinas, N.; Tabachnikov, O.; Landau, M. Staphylococcus Aureus PSMα3 Cross-α Fibril Polymorphism and Determinants of Cytotoxicity. *Structure* **2020**, *28* (3), 301-313.e6. https://doi.org/10.1016/j.str.2019.12.006.